

# Elastodynamic analysis of anisotropic elastic solid with multiple nanocavities

Sonia Parvanova<sup>a</sup>, Georgi Vasilev<sup>a</sup>  and Petia Dineva<sup>b</sup>

<sup>a</sup>Department of Structural Engineering, University of Architecture, Civil Engineering and Geodesy (UACEG), Sofia, Bulgaria; <sup>b</sup>Institute of Mechanics, Bulgarian Academy of Sciences (BAS), Sofia, Bulgaria

## ABSTRACT

2D elastodynamic problem for a finite elastic anisotropic solid with nanosized cavities is worked out in this paper. The solid under plane strain conditions is subjected to time-harmonic load. The developed computational tool for the steady-state problem is boundary integral equation method based on frequency-dependent fundamental solutions for elastic anisotropic continuum obtained by Radon transform. Accuracy of the dynamic stress concentration factor and displacement components is proven by comparisons with existing in the literature analytical solution and with the results obtained using commercial finite element package. In addition, a parametric study is performed in order to examine the sensitivity of the dynamic stress concentration field to the geometrical configuration of multiple cavities, to the characteristics of the surface elastic properties, to the type of orthotropy and to the dynamic interaction between cavities.

## ARTICLE HISTORY

Received 13 October 2015  
Accepted 31 March 2016

## KEYWORDS

Elastodynamics;  
nanocavities; plane strain  
state; general anisotropy;  
frequency domain; Radon  
transform; dynamic stress  
concentration factor (DSCF)

## 1. Introduction

The static and dynamic behaviour of a heterogeneous or composite solid containing multiple inclusions and/or cavities is an important engineering problem with applications in many modern technological fields such as material science, non-destructive evaluation, computational geophysics and fracture mechanics (Meguid & Wang, 1995; Dineva, Rangelov, & Gross, 2005; Garcia-Sanchez, 2005; Garcia-Sanchez, Saez, & Dominguez, 2006; Dineva, Rangelov, Manolis, & Wuttke, 2014a; Dineva, Gross, Muller, & Rangelov, 2014b; Datta & Shah, 2008; Grekov & Morozov, 2012; Rizov, 2014, 2015). Propagation of elastic waves through heterogeneous material causes reflection, refraction, diffraction and scattering phenomena that are difficult to quantify. In addition, different types of discontinuities such as cracks, cavities and inclusions further complicate the overall wave picture by acting as scatterers and stress concentrators. Prediction of the dynamic

response of a finite elastic anisotropic heterogeneous solid with defects from nano to macroscales is very important for the safe operation and optimum design of the engineering structures subjected to dynamic loads. At the same time, this is a difficult issue involving complex mechanical models that demand high performance computational tools and advanced research software. Nanomaterials are reported to be the materials of twenty-first century with respect to their unique design and property combinations that are not found in conventional ones. When the characteristic cross-section dimension of the considered solid gets much lower than microns, the ratio of the surface area to volume becomes more prominent, thus the solid is strongly influenced by its surface characteristics which lead to distinct mechanical properties compared with their bulk counterpart. With the rapid development of nanomechanical systems, the size-dependent phenomena in the scattered wave field in nanostructures with defects as cavities and inclusions need to be sufficiently understood and have attracted widespread interest. The variation in surface energy of the nanostructures is caused by the fact that the bonds of the surface atoms are relaxed and this lead to formation of surface residual stress which does not happen inside the solid core. Such specific behaviour is termed as the surface stress effect and in the surface model introduced by Gurtin and Murdoch (1975, 1978) and Gurtin, Weissmuller, and Larche (1998), the surface stress is the summation of the surface residual stress and surface elasticity. In this model, the interfaces between the nanoinhomogeneity and the matrix are regarded as material thin surfaces that possess their own mechanical properties and surface tension. For structures with sizes greater than 100 nm, the surface-to-volume ratio is negligible and the effective properties are governed by classical bulk elastic strain energy through a fourth-order elastic stiffness tensor. In opposite, the strain energy can be dramatically altered by surface effects which are in the base of the nanotechnology.

What follows is a short authors' review of the results existing in the literature limited only to two-dimensional in-plane problems for heterogeneous materials with cavities and inclusions at nanoscale under dynamic loads basing on the Gurtin-Murdoch model.

In-plane wave motion problems for diffraction of time-harmonic P- and SV-waves by nanoholes and nanoinclusions were studied analytically in Wang (2009); Zhang, Wang, and Schiavone (2011); Wang, Wang, and Feng (2006) and Ru, Wang, and Wang (2009). Using the wave function expansion method, the analytical expressions of wave diffraction field in an infinite elastic isotropic plane with two circular holes were derived in Wang (2009). In Wang et al. (2006), the diffraction of plane harmonic compressional P-wave by a nanosized circular hole was considered using the same method. It was also applied in Zhang et al. (2011) in order to study the diffraction of elastic waves by an array of cylindrical holes including the effects of surface elasticity. The diffractions of plane longitudinal P-waves and shear SV-waves by a cylindrical nanohole and nanoinclusion were investigated in Ru et al. (2009). Fang, Liu, Yang and Zhang (2010) evaluated

analytically the effect of surface/interface on the dynamic stress around single circular cavity, single circular inclusion and two interacting circular nanoinclusions in infinite matrix under P-waves.

Generally speaking, numerical techniques are now thought of as being the preferred way for studying elastic wave motion in heterogeneous media. Among currently used numerical approaches, BIEM has become quite popular over the last decade because of its efficient handling of heterogeneous materials reformulating the corresponding boundary-value problem by integral equations only along the existing boundaries via the usage of reciprocity theorem and fundamental solution (FS) of the governing equation. The following conclusions could be made from the above short review: (i) to date, there is still a lack of results concerning the surface effects on the dynamical behaviour of elastic anisotropic solids; (ii) most of the used computational techniques for isotropic solids are analytical, there are few papers presenting BIEM as an efficient tool for solution of mechanical problems at nanoscale and they all concern static solutions (Dong & Pan, 2011; Dong, 2012; Jammes, Mogilevskaya, & Crouch, 2009; Mogilevskaya, Crouch, & Stolarski, 2008), except the authors' results, see Parvanova, Manolis, and Dineva (2015) and Parvanova, Vasilev, Dineva, and Manolis (2016), who treat dynamic problems of elastic isotropic solids; (iii) to the best of the authors' knowledge, there are no results for solution of the dynamic problems for finite anisotropic solids with a cavity subjected to dynamic time-harmonic load.

The present work aims to propose a systematic BIEM study on this problem, namely the dynamic response of a finite anisotropic solid with multiple nanocavities, and it can be viewed as a continuation of previous work of the authors (Parvanova et al., 2015, 2016). The main goals are: (i) To solve two-dimensional elastodynamic problem in frequency domain for a finite anisotropic elastic solid with multiple, arbitrary in number and mutual disposition cavities at nanoscale; (ii) To develop, verify and insert in numerical simulations an efficient boundary integral equation method and accompanied software based on the reciprocity theorem, frequency-dependent elastodynamic fundamental solutions and discretisation and collocation techniques for reducing the problem to solution of linear algebraic system of equations with respect to the unknown field variables.

The paper is organised as follows: the formulation of the considered two-dimensional in-plane elastodynamic problem for a finite general anisotropic solid at nanoscale with multiple cavities and subjected to dynamic load is presented in Section 2, while its reformulation via boundary integral equations along existing boundaries in the solid based on the analytically derived by Radon transform fundamental solution is given in Section 3. Verification of the proposed numerical scheme is shown in Section 4, and a parametric study revealing some new size-dependent effects is presented in Section 5. Finally conclusions are discussed in the last Section 6.

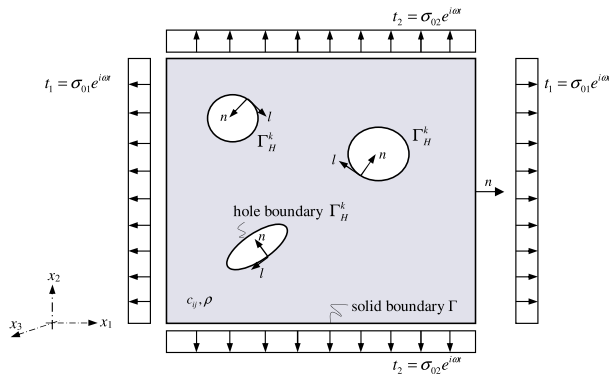


**Figure 1.** The problem geometry: anisotropic finite plate with multiple cavities.

## 2. Problem Formulation

In a Cartesian coordinate system  $Ox_1x_2x_3$  in the plane  $x_3 = 0$  consider an anisotropic finite plate with boundary  $\Gamma$  subjected to time-harmonic loads with frequency  $\omega$ , see Figure 1. The solid matrix contains a set of  $N$  nanocavities with boundaries  $\Gamma_H^k$ , where  $k = 1, 2, \dots, N$ , of arbitrary shape, number, size and configuration. The heterogeneities do not intersect each other and their total surface is denoted as  $\Gamma_H = \bigcup_{k=1}^N \Gamma_H^k$ . It is assumed that anisotropic material is of monoclinic type (there exists at least one elastic symmetry plane), because this is the necessary condition for uncoupling of the 3D problem to two-dimensional ones: in-plane and anti-plane, Garcia-Sanchez (2005). Plane strain state, i.e. in-plane wave motion with respect to plane  $x_3 = 0$  is considered. In this case, the only non-zero field quantities are displacements  $u_1, u_2$ , stresses  $\sigma_{11}, \sigma_{12}, \sigma_{22}$  and tractions  $t_i = \sigma_{ij}n_j$ ,  $i, j = 1, 2$ , all dependent on coordinates  $\mathbf{x} = (x_1, x_2)$  and frequency  $\omega$ , where  $n_j$  is the outward pointing unit normal vector to the surface. In what follows is the definition of the boundary-value problem (BVP) by the governing partial differential equations of elastodynamics in frequency domain and corresponding boundary conditions.

### 2.1. Governing equations in the bulk solid

#### 2.1.1. Constitutive equation (Hooke's law)

In the case of general anisotropy, the angle  $\chi$  between the coordinate axes  $Ox_2$  and the principal axes of the material symmetry  $Ox'_2$  is  $\chi \neq 0; \pi/2$  and in this case six parameters  $c_{11}, c_{12}, c_{16}, c_{22}, c_{26}$  and  $c_{66}$  characterise the stiffness tensor. Note that the contracted notation of Voigt (1910) is applied to the fourth-order stiffness tensor  $C_{ijkp}$  where  $C_{ijkl} = C_{jikl} = C_{ijlk} = C_{klij}$ ,  $C_{ijk}g_{ij}g_{kl} > 0$  for any non-zero real symmetric tensor  $g_{ij}$ . In this case, the Hooke's law is presented in the following matrix form:

$$\begin{Bmatrix} \sigma_{11} \\ \sigma_{22} \\ \sigma_{12} \end{Bmatrix} = \begin{bmatrix} c_{11} & c_{12} & c_{16} \\ c_{12} & c_{22} & c_{26} \\ c_{16} & c_{26} & c_{66} \end{bmatrix} \begin{Bmatrix} \varepsilon_{11} \\ \varepsilon_{22} \\ 2\varepsilon_{12} \end{Bmatrix} \quad (1)$$

If the principal axis of the material symmetry  $Ox'_2$  coincides with the coordinate axis  $Ox_2$ , the material is orthotropic and it is characterised with the following four independent material constants  $c_{11}$ ,  $c_{12}$ ,  $c_{22}$  and  $c_{66}$ , because  $c_{16} = c_{26} = 0$ . The orthotropic case is transformed into isotropic one if the subsequent relations are truth  $c_{11} = c_{22} = \lambda + 2\mu$  and  $c_{12} = \lambda$ ;  $c_{66} = \mu$ , where  $\lambda$  and  $\mu$  are Lamé constants. Coefficients  $c_{ij}$  should satisfy the following conditions for positive strain energy and real and positive wave velocities:  $c_{11} > |c_{12}|$ ,  $(c_{11} + c_{12})c_{22} > 2(c_{12})^2$ ,  $c_{66} > 0$ ,  $c_{11} > 0$ ,  $c_{22} > 0$ ,  $|c_{12} + c_{66}| < (\sqrt{c_{11}c_{22}} + c_{66})$ .

### 2.1.2. Kinematics relations under assumption of small displacements

$$\varepsilon_{ij} = \frac{1}{2} (u_{i,j} + u_{j,i}) \quad i, j = 1, 2, \quad (2)$$

where  $\varepsilon_{ij}$  is the strain tensor, comma subscripts denote partial differentiation with respect to the spatial coordinates and the summation convention over repeated indices is implied.

### 2.1.3. Equation of motion in plane $x_3 = 0$ and in the absence of body forces

$$\sigma_{ij,j}(\mathbf{x}, \omega) + \rho\omega^2 u_i(\mathbf{x}, \omega) = 0, \quad (3)$$

here  $\rho$  is the mass density. In Equations (1–3),  $c_{ij}$  and  $\rho$  are stiffness tensor and mass density of the solid matrix material.

## 2.2. Boundary conditions

At any point along the cavity interface  $\Gamma_H = \bigcup_{k=1}^N \Gamma_H^k$  we can define unit outward normal vector  $n$  (see Figure 1) and unit tangential vector  $l$  such that  $(n, l, x_3)$  forms right-handed coordinate system. The traction  $t_i$  at any point  $\mathbf{x}$  on the line segment with normal vector  $\mathbf{n}$  is defined as  $t_i = \sigma_{ij}n_j$ .

Boundary conditions along external boundary  $\Gamma$  of the rectangular finite plate, where a prescribed time-harmonic traction is applied, are as follows:

$$t_j(\mathbf{x}, \omega) = \sigma_{0j}(\mathbf{x})e^{i\omega t}, \quad j = 1, 2, \mathbf{x} \in \Gamma \quad (4)$$

where  $\sigma_{0j}$  is the magnitude of the applied loads in both directions, see Figure 1.

Boundary conditions along the cavity interface  $\Gamma_H$  at macro-level hold:

$$t_j(\mathbf{x}, \omega) = 0, \quad j = 1, 2, \mathbf{x} \in \Gamma_H \quad (5)$$

Non-classical boundary conditions along the cavity interfaces  $\Gamma_H$  express a jump of stresses from the matrix to cavity surfaces due to the presence of surface stress  $\sigma_{ij}^S$  along each cavity interface  $s_k \equiv \Gamma_H^k$

$$\sigma_{ij}^S = \tau_0 \delta_{ij} + \frac{\partial E}{\partial \varepsilon_{ij}^S} \quad (6)$$

The surface stress  $\sigma_{ij}^S$  is related to the deformation-dependent surface energy  $E$ , where  $\varepsilon_{ij}^S$  is the  $2 \times 2$  strain tensor for the surface  $s_k \equiv \Gamma_H^k$ ,  $\delta_{ij}$  is the Kronecker delta symbol,  $\tau_0$  is the residual surface tension under unstrained condition (along undeformed interface boundary) which is independent of deformation and induce an additional static deformation. The residual surface tension  $\tau_0$  is often ignored in the dynamic analysis. Following the surface elasticity theory of Gurtin and Murdoch (1975), the  $k$ -th interface along the relevant cavity contour is regarded as a thin material film with its own mechanical properties  $\lambda^{S,k}$ ,  $\mu^{S,k}$ , different from that of the surrounding matrix, and surface tension  $\tau_0^k$ . Each thin surface layer is assumed to be isotropic and all hole surfaces have identical material properties, denoted by  $\lambda^S$ ,  $\mu^S$ ,  $\tau_0$ . The surface equilibrium conditions along the arc length  $s_k$ , i.e. on the undeformed  $k$ -th hole interface  $\Gamma_H^k$ , written in terms of the local normal and tangential ( $n, l$ ) coordinates defined on  $s_k$  (see Mogilevskaya et al., 2008; Dong & Pan, 2011) are:

$$\begin{aligned} \sigma_{nl}^M &= -\left( \frac{\partial \sigma_{ll}^S}{\partial l} + \frac{\tau_0 \psi_{ll}^S}{\tilde{\rho}} \right) \\ \sigma_{nn}^M &= -\left( -\frac{\sigma_{ll}^S}{\tilde{\rho}} + \tau_0 \frac{\partial \psi_{ll}^S}{\partial l} \right) \end{aligned} \quad (7)$$

$$\psi_{ll}^S = -\frac{u_l}{\tilde{\rho}} + \frac{\partial u_n}{\partial l} \quad (8)$$

Here:  $\sigma_{ll}^S = \tau_0 + (\lambda^S + 2\mu^S) \varepsilon_{ll}^S$  is the stress in tangential direction expressed by the constitutive equation for elastic isotropic behaviour of the thin interface layer,  $\tilde{\rho}$  is the curvature radius of the interface boundary  $s_k$ ,  $(u_n, u_l)$  are the displacement components in the local coordinate system ( $n, l$ ). The superscript  $M$  indicates solid matrix domain. A coherent interface  $s_k$  is considered (perfect bonded, no slip, twist or wrinkling), where the strain  $\varepsilon_{ll}^S$  in tangential direction  $l$  is equal to the associated tangential strain in the abutting bulk matrix  $\varepsilon_{ll}^M$ , i.e.  $\varepsilon_{ll}^S = \varepsilon_{ll}^M$ . In this case the following condition is satisfied

$$\varepsilon_{ll}^S = \frac{u_n}{\tilde{\rho}} + \frac{\partial u_l}{\partial l} \quad (9)$$

Boundary conditions (6–9) could be reformulated in a more compact form with respect to the tractions developed along the hole interface boundary as seen from the matrix domain, see Dong and Pan (2011) and Parvanova et al. (2015):

$$\begin{Bmatrix} t_1^M \\ t_2^M \end{Bmatrix} = \{\mathbf{f}^S\} + [\mathbf{T}^S] \begin{Bmatrix} u_1 \\ u_2 \end{Bmatrix} \quad \text{on } S \quad (10)$$

$$\{\mathbf{f}^S\} = \frac{\tau_0}{\tilde{\rho}} \begin{Bmatrix} n_1 \\ n_2 \end{Bmatrix} \quad (11)$$

$$[\mathbf{T}^S] = \mathbf{T}_1 + \frac{\partial}{\partial l} \mathbf{T}_2 + \frac{\partial^2}{\partial l^2} \mathbf{T}_3 \quad (12)$$

$$[\mathbf{T}_1] = \begin{bmatrix} n_1 & -n_2 \\ n_2 & n_1 \end{bmatrix} \begin{bmatrix} -\frac{\alpha}{\tilde{\rho}^2} & \frac{\tau_0}{\tilde{\rho}^2} \frac{\partial \tilde{\rho}}{\partial l} \\ -\frac{\alpha}{\tilde{\rho}^2} \frac{\partial \tilde{\rho}}{\partial l} & -\frac{\tau_0}{\tilde{\rho}^2} \end{bmatrix} \begin{bmatrix} n_1 & n_2 \\ -n_2 & n_1 \end{bmatrix} \quad (13)$$

$$[\mathbf{T}_2] = \begin{bmatrix} n_1 & -n_2 \\ n_2 & n_1 \end{bmatrix} \begin{bmatrix} 0 & -\beta \\ \beta & 0 \end{bmatrix} \begin{bmatrix} n_1 & n_2 \\ -n_2 & n_1 \end{bmatrix} \quad (14)$$

$$[\mathbf{T}_3] = \begin{bmatrix} n_1 & -n_2 \\ n_2 & n_1 \end{bmatrix} \begin{bmatrix} \tau_0 & 0 \\ 0 & \alpha \end{bmatrix} \begin{bmatrix} n_1 & n_2 \\ -n_2 & n_1 \end{bmatrix} \quad (15)$$

Where:  $\alpha = \lambda^S + 2\mu^S$ ,  $\beta = (\alpha + \tau_0)/\tilde{\rho}$ ,  $\partial/\partial l$  and  $\partial^2/\partial l^2$  are the first and second tangential derivatives respectively. Note that when  $\tau_0 = \lambda^S = \mu^S = 0$  the boundary condition (10) transforms into classical boundary condition (5) describing the traction equilibrium. The superscript  $M$  indicates solid matrix domain with the positive unit outward normal vector as shown in Figure 1.

Finally, the BVP for a finite anisotropic plate containing cavities and subjected to harmonic in time load is presented by the governing Equation (3) and the following boundary conditions for: (i) macro-cavity-(4), (5); (ii) nano-cavity-(4), (10).

### 3. BIEM formulation

The formulated BVP in Section 2 can be described in the case of time-harmonic load by the following frequency-dependent BIEs along the external solid boundary  $\Gamma$  and cavity interfaces  $\Gamma_{Hp}$  following Brebbia (1978) and Dominguez (1993):

$$c_{ij}u_j(\mathbf{x}, \omega) = \int_{\Gamma \cup \Gamma_H} U_{ij}^*(\mathbf{x}, \boldsymbol{\xi}, \omega) t_j(\boldsymbol{\xi}, \omega) d\xi - \int_{\Gamma \cup \Gamma_H} T_{ij}^*(\mathbf{x}, \boldsymbol{\xi}, \omega) u_j(\boldsymbol{\xi}, \omega) d\xi \quad (16)$$

Here:  $\mathbf{x} \in \Gamma \cup \Gamma_H$ ;  $c_{ij}$  is the jump term depending on the local geometry at the collocation point  $\mathbf{x}(x_1, x_2)$ ; the couple  $\mathbf{x}, \boldsymbol{\xi}$  presents the position vectors of the source and receiver, respectively;  $U_{ij}^*(\mathbf{x}, \boldsymbol{\xi}, \omega)$  is the displacement fundamental solution of the governing elliptic partial differential Equation (3) for in-plane wave motion in generally anisotropic solid, and its corresponding traction is  $T_{ij}^*(\mathbf{x}, \boldsymbol{\xi}, \omega) = C_{ijql} U_{qk,l}^*(\mathbf{x}, \boldsymbol{\xi}, \omega) n_k$ , see the Appendix A.

## 4. Verification study

### 4.1. Test example 1: nanoscale circular cavity in an isotropic matrix under static uniform load

Consider a square elastic isotropic matrix of size  $100a_0$  containing a circular cavity of radius  $a_0 = 1.10^{-9}\text{m}$ . The elastic isotropic properties of the matrix are as follows: Lamé constants are  $\lambda_M = 64.43 \text{ GPa}$ ,  $\mu_M = 32.9 \text{ GPa}$  and the equivalent stiffness tensor assigned in the computer code is  $c_{11} = c_{22} = \lambda + 2\mu$ ,  $c_{12} = \lambda$ ,  $c_{66} = \mu$ ,  $c_{16} = c_{26} = 1e - 6$ . The first numerical example is for isotropic material but the results presented below are obtained using fundamental solutions for anisotropic one. The far field loading is the static equivalent of a longitudinal P-wave, namely the vertical edges of the square matrix are subjected to uniform normal tractions  $t_1 = \sigma_0$ , whereas the horizontal edges have normal tractions  $t_2 = \sigma_0 \nu / (1 - \nu)$ . The excitation frequency is low and equal to  $1e-4 \text{ rad/s}$ , in order to simulate quasi-static conditions. The surface stresses acting at the cavity's boundary are modelled as an elastic isotropic thin film with surface parameters  $\lambda^S$  and  $\mu^S$ . Surface effects are defined by parameter  $K_S = 2\mu^S + \lambda^S - \tau^0$ , and the special case of  $\tau^0 = 0$  is used in the verification study.

The benchmark solution is for an infinite elastic isotropic plane with a single, nanoscale cylindrical cavity under the described above far-field loading. The matrix size of  $100a_0$  is sufficiently large to rule out the influence of the external boundaries on the near field around the cavity. This test example was solved analytically in Grekov and Morozov (2012), who reduced the BVP to a hypersingular integral equation with respect to the unknown surface stress by applying the Goursat-Kolosov complex potential theory and Muskhelishvili's technique. Figure 2 is a comparison between our BIEM results and the analytical solution in Grekov and Morozov (2012) for the normalised hoop stress  $\sigma_{\varphi\varphi}/\sigma_0$  along the perimeter of the circular cavity with fixed radius  $a_0$  and for different values of parameter  $K_S$  (in N/m). The BIEM mesh comprised 16 quadratic boundary elements (BE) for the cavity boundary and 16 quadratic BE for the square matrix, with 4 BE per side. We observe that the BIEM solution reproduces the analytical solution extremely

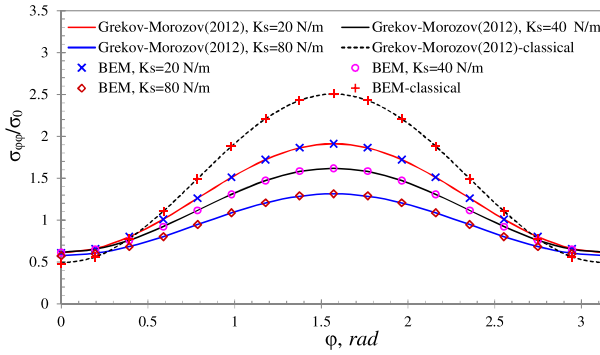


**Figure 2.** Dimensionless hoop stress  $\sigma_{\varphi\varphi}/\sigma_0$  along the circular cavity perimeter for different surface elastic  $K_s$  values.

well. More specifically, the percentage errors vary between 0.01 and 0.61% for all polar angles and surface parameters.

#### 4.2. Test example 2: circular cavity in a square orthotropic matrix under a dynamic load

The aim of the present verification example is to prove the accuracy of the above-discussed BIEM numerical scheme for the elastodynamic behaviour of homogeneous anisotropic solid at macroscale and those generated by the FEM software ANSYS. To the authors' best knowledge, there are no BIEM results based on fundamental solution for anisotropic material with nano-inclusions/nanocavities. The surface stress effects around the cavity are neglected in the current model and only the classical solutions are compared since a number of verification examples involving interface stress effects have been already reported by the authors for the isotropic media, see Parvanova et al. (2015, 2016). Its application for anisotropic matrix is the same.

The model under consideration is a square plate with a single circular cavity at its centre under time harmonic tensile forces of magnitude  $\sigma_0$  applied in horizontal direction (Figure 6(a)). The diameter of the cavity is  $d = 2a_0$  and the size of the square plate is  $10d$ . Material parameters of the matrix are for orthotropic material, see Ohyoshi (1973), given as a ratio of  $c_{11}$ . The stiffness tensor is defined as  $c_{11} = s_{ij}c_{11}$ , where in the present numerical example  $a_0 = 1$ ,  $c_{11} = 1$  and  $\rho = 1$  in consistent units. The following cases with respect to the ration  $s_{ij}$  are considered: orthotropic material type (1)  $s_{11} = 1$ ,  $s_{12} = 1/3$ ,  $s_{22} = 1$ ,  $s_{66} = 1/6$ ; orthotropic material type (2)  $s_{11} = 1$ ,  $s_{12} = 1/30$ ,  $s_{22} = 1$ ,  $s_{66} = 1/3$ . The normalised frequencies are equal to  $\Omega = \omega d \sqrt{\rho/c_{66}} = 0.49$  and  $\Omega = 0.416$  for the first and the second material types, respectively. There is no material damping in the numerical model.

The results obtained by both numerical techniques are plotted in Figures 3 and 4. More specifically, Figure 3(a) plots the displacement component amplitudes

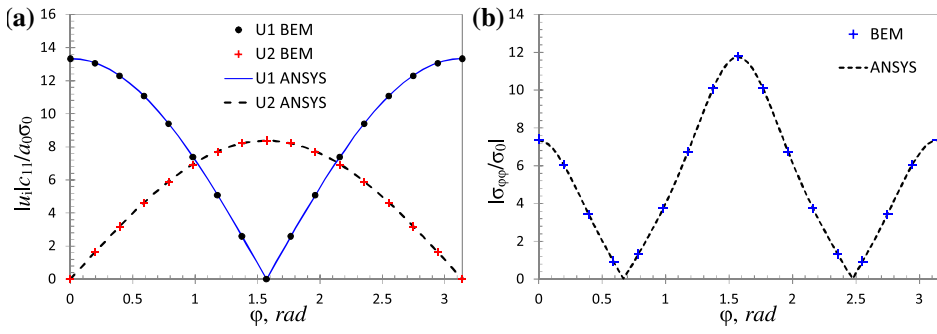


**Figure 3.** Single circular cavity in a square plate of orthotropic material type (1): (a) normalised horizontal and vertical displacement components versus polar angle; (b) normalised hoop stresses along the cavity contour.

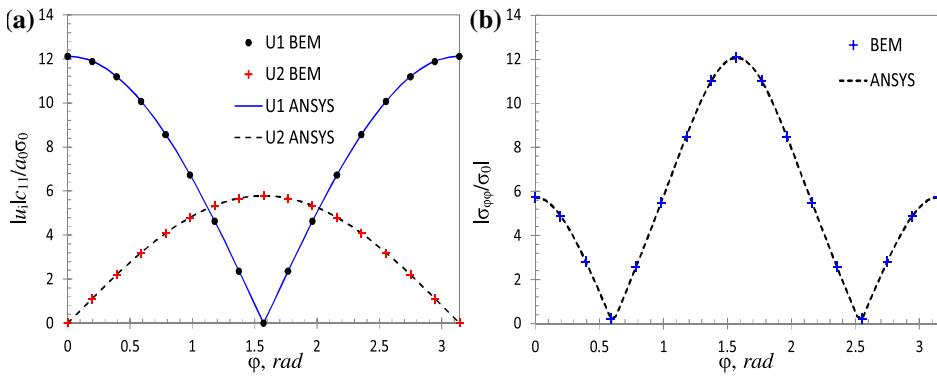


**Figure 4.** Single circular cavity in a square plate of orthotropic material type (2): (a) normalised displacement components versus polar angle; (b) normalised hoop stresses along the cavity contour.

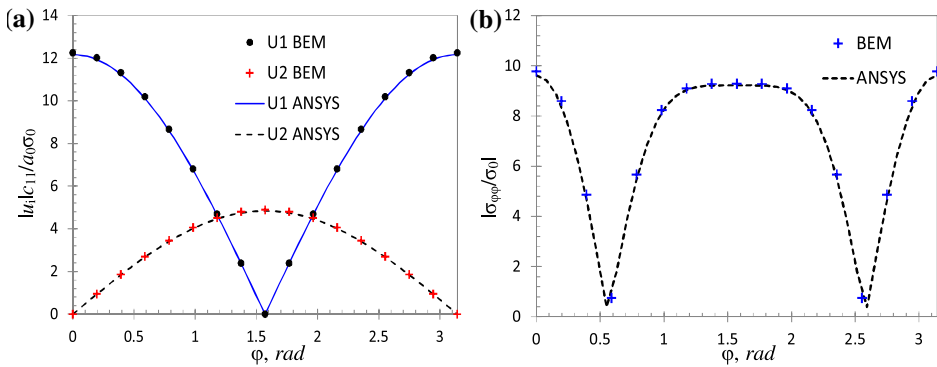


**Figure 5.** Single circular cavity in a square plate of orthotropic material type (3): (a) normalised displacement components versus polar angle; (b) normalised hoop stresses along the cavity contour.

normalised as  $|u_i|c_{11}/a_0\sigma_0$ ,  $i = 1, 2$ , Figure 3(b) depicts the normalised hoop stresses  $|\sigma_{\varphi\varphi}/\sigma_0|$  versus polar angle  $\varphi$  for the first material type. The same set of results, for the second orthotropic material, is given in Figure 4. The percentage difference in the peak values of the normalised horizontal and vertical displacement components, obtained by the BEM and FEM solutions, are 0.15 and 0.2%, respectively, for the first material type and 0.14 and 0.25% for the second one. The percentage differences in the peak values of the normalised stresses (at  $\varphi = 0$  and  $\varphi = \pi/2$  in Figure 3(b)) are 0.53 and 0.38% for the first material. The same differences for the second material (Figure 4(b)) are 0.17 and 0.09%, respectively. The percentage differences are calculated with respect to the average BEM/FEM values, since both are numerical methods and could be considered as having comparable accuracy. The BEM mesh consists of 16 quadratic BE for the cavity's boundary and 16 quadratic BE for the square plate contour. In order to achieve plotting accuracy in the hoop stresses in Figures 3(b) and 4(b), respectively, the FEM mesh needs to be much finer than the corresponding BEM mesh and much finer than the relevant finite element (FE) mesh for isotropic materials. With other words, in case of anisotropy the FEM convergence rates for displacements and stresses are different and convergence of stresses requires finer mesh. In the present numerical examples, the FE mesh is structured so as to have 160 quadratic, planar FE along the cavity contour, which results in 320 boundary nodes. The plate edges are discretised into 60 FE and finally the entire mesh comprises 9004 quadratic, eight-noded plane FE (PLANE 82). Otherwise, the percentage differences in stresses are larger than 1%. More specifically with 80 quadratic FE along the cavity contour the BEM (16 BE for cavity perimeter)/FEM differences in the observed peak stresses are 2.02 and 1.80%, while with 40 quadratic FE along the cavity the same differences are 6.22 and 5.96%.

Additional verification example is done for the following orthotropic material  $c_{11} = 1,57 \cdot 10^9 \text{Pa}$ ,  $c_{12} = 1,26 \cdot 10^9 \text{Pa}$ ,  $c_{22} = 4,17 \cdot 10^9 \text{Pa}$ ,  $c_{66} = 1 \cdot 10^9 \text{Pa}$ , the density is  $1570 \text{kg/m}^3$ , with data taken from Chuhan, Yuntao, Pekau, and Feng (2004). Here  $c_{11} \neq c_{22}$ , which was not fulfilled for the previous orthotropic materials. The numerical model loading and geometrical dimensions are the same as those of the previous two verification examples. The normalised frequency is  $\Omega = 0.26$ .

The obtained results are plotted in Figure 5. More specifically, Figure 5(a) plots the displacement component amplitudes normalised as  $|u_i|c_{11}/a_0\sigma_0$ ,  $i = 1, 2$ , Figure 5(b) depicts the normalised hoop stresses  $|\sigma_{\varphi\varphi}/\sigma_0|$  versus polar angle  $\varphi$ . All differences between BEM and FEM solutions are less than 1%. The FEM mesh is the same as before, the BEM mesh consists of 16 quadratic BE for the cavity's boundary and 48 quadratic BE for the square plate contour.

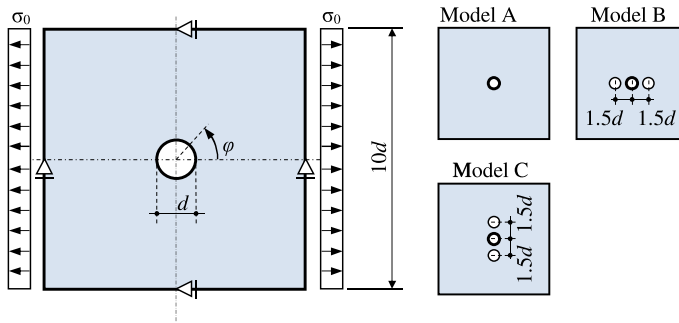


**Figure 6.** Orthotropic square plate with various cavity configurations: Geometry, dimensions and layouts for Models A–C.

## 5. Parametric study

In this section, we consider three different cavity configurations in a finite square elastic orthotropic plate at nanoscale (Figure 6) subjected to uniform time-harmonic load with magnitude  $\sigma_0$  along horizontal direction.

The aim here is to quantify dynamic stress concentration factor (DSCF) dependence in case of anisotropic matrix to the following key factors: (i) surface properties, as quantified by the interfacial material constants; (ii) dynamic interactions between multiple nanocavities, including the external boundary of the elastic matrix and (iii) cavities' configuration. The second target is to compare the present conclusions with those observed in the case of isotropic matrix reported in recent publications of the authors (Parvanova et al. (2015, 2016).

In all numerical simulations, the solid matrix is a square plate made of orthotropic material. Three basic cavity configurations are considered: single cavity at the centre of the plate (model A); three horizontal (model B) and three vertical (model C) cavity arrangements as shown in Figure 6. The geometrical dimensions and material properties are the same as those in the second verification example. The dimensionless parameter which captures interface effects at the nanoscale is defined as  $s = K_s/c_{66}d$ , where  $c_{66}$  is the stiffness tensor component of the square plate material. Dimensionless parameter  $s$  is introduced in the papers of Wang et al. (2006), Wang (2009) and Ru et al. (2009) to better gauge interface effects at the nanoscale. More specifically, a macroscopic cavity with large diameter leads to  $s \ll 1$  values, and surface effects can be neglected. However, when the radius of the cavity shrinks to the nanoscale,  $s$  becomes noticeable and the surface effect should be considered in analysis. The dimensionless parameter  $s$  allows us to fix the radius of the cavity and to vary  $K_s$  in order to achieve nanoscale problem or vice versa to fix the surface elasticity parameters and change the radius of the cavity. In both cases nanoscale is reached and influence of the applied surface model is noticeable when  $s$  is larger than 0.05, and this is reported in Parvanova et al. (2015, 2016). The excitation frequency is fixed and corresponds to normalised values of  $\Omega = \omega d \sqrt{\rho/c_{66}} = 0.5$  for the first material type and  $\Omega = 0.4$  for the second one.

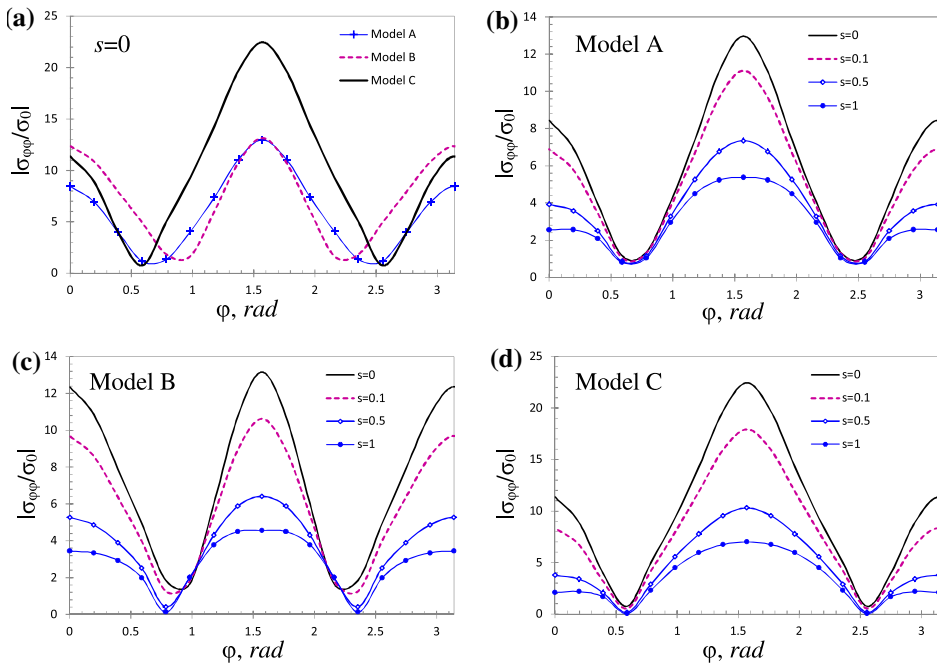


**Figure 7.** Square plate of orthotropic material (1): (a) DSCF at the central cavity for all models at fixed surface parameter  $s=0$ ; (b–d) normalised hoop stresses on the central cavity perimeter for models A–C.

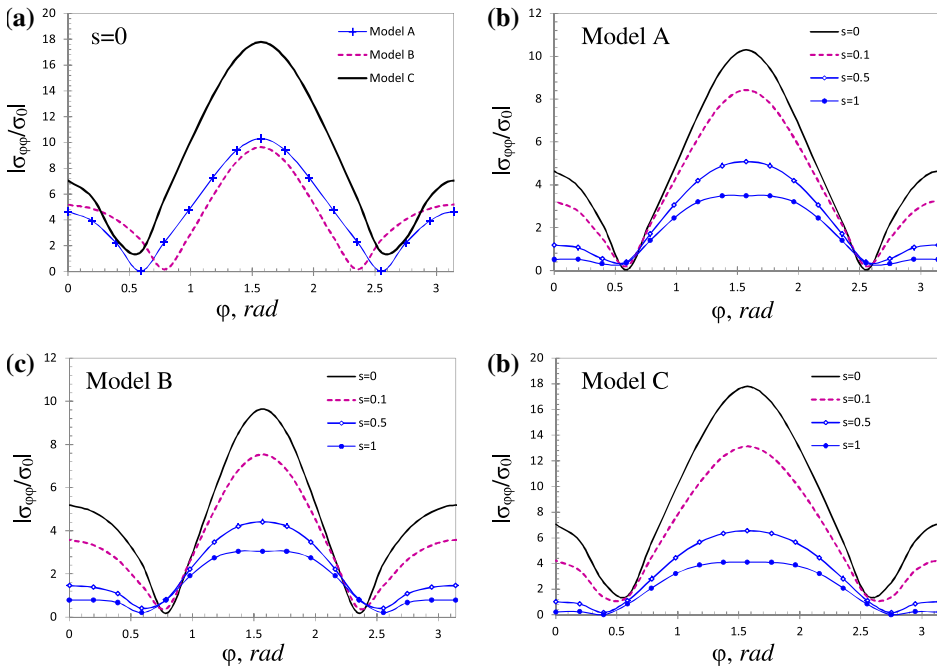


**Figure 8.** Square plate of orthotropic material (2): (a) DSCF at the central cavity for all models at fixed surface parameter  $s=0$ ; (b–d) normalised hoop stresses on the central cavity perimeter for models A–C.

All simulation results for the first orthotropic material type are depicted in Figure 7. More specifically, Figure 7(a) plots the DSCF defined as  $|\sigma_{\varphi\varphi}/\sigma_0|$  at the central cavity perimeter for models A–C in the absence of surface stress effects ( $s = 0$ ). Sub-Figure 7(b)–(d) show the DSCF for cavity arrangements A–C, respectively, for various values of surface normalised interface stress effects ranging from 0 to unity. The same set of results for the second orthotropic material is illustrated in Figure 8. Finally, we would like to note that although the presented results are for orthotropic materials, the fundamental solution inserted in the authors' BEM software is for general anisotropic material. The numerical scheme developed, verified and inserted in simulations by the authors allows computations not only for orthotropic materials.

Comparing the current results with those obtained for similar cavity arrangements but in an isotropic square plate (Parvanova et al., 2016) the following conclusions could be made: (i) Three horizontal cavities arrangement does not change (Figure 7(a)) or slightly reduces (Figure 8(a)) the DSCF in the central cavity, while in case of isotropic material substantial reduction in the hoop stresses was observed; (ii) Three vertical cavities arrangement lead to the considerable amplification of more than 50% in the DSCF at the central cavity perimeter in case of orthotropic materials (Figures 7(a) and 8(a)). Similar effects are observed in case of isotropic materials but the order of amplification there is smaller; (iii) The influence of the surface parameter  $s$  to the stress distribution around the central cavity is identical to that observed in case of isotropic material. The strong influence of the surface parameter (resp. the size of the cavities) on the stress concentration field is visible for both anisotropic materials. With the increase in the surface parameter  $s = K_s/c_{66}d$  the DSCF decreases and thus the effects at the nanoscale are clearly demonstrated.

All figures in the parametric study demonstrate the combined effect of: the orthotropy; heterogeneity type, size, number and geometry; the dynamic load type and characteristics on the stress concentration fields.

## 6. Conclusions

Numerical solution for 2D, in-plane time-harmonic wave motion that develops in a finite-sized elastic anisotropic solid containing multiple cylindrical cavities at nanolevel of arbitrary size, geometrical configuration and elastic properties is presented in the paper. The computational tool is the BIEM based on the frequency-dependent fundamental solution derived by Radon transform for general anisotropic continua. This yields an effective numerical scheme, and the accompanied research software which is developed for finite anisotropic solids with nanocavities.

The numerical results obtained show a marked dependence of the non-uniform stress and displacement fields to the size of the cavities, their number and position, as well as their mutual interaction with the incoming elastic waves propagating

in finite anisotropic solids. The results are summarised by tracing the influence of the cavities on the ensuing DSCFs.

The numerical simulations demonstrate the potential of the BIEM to produce highly accurate results regarding the dynamic behaviour of finite anisotropic solids strengthened (or weakened) by multiple cavities at macro and nanolevel, with marked economy as compared to the standard engineering analysis employing finite elements.

### Disclosure statement

No potential conflict of interest was reported by the authors.

### Funding

This work was supported by the Bulgarian NSF [grant number DFNI-I02/12].

### ORCID

Georgi Vasilev  <http://orcid.org/0000-0002-2835-9520>

### References

- Brebbia, C. A. (1978). *The BEM for engineers*. London: Pentech Press.
- Chuhan, Z., Yuntao, R., Pekau, O. A., & Feng, J. (2004). Time-domain boundary element method for underground structures in orthotropic media. *Journal of Engineering Mechanics*, 130, 105–116.
- Datta, S. K., & Shah, A. H. (2008). *Elastic waves in composite media and structures*. With applications to ultrasonic nondestructive evaluation: Mechanical and Aerospace Engineering Series, eBook 1–336. Boca Raton, FL: CRC Press. ISBN 978-1-4200-5339-5.
- Denda, M., Wang, C. Y., & Yong, Y. K. (2003). 2-D time harmonic BEM for solids of general anisotropy with application to eigenvalue problems. *Journal of Sound and Vibration*, 261, 247–276.
- Dineva, P., Gross, D., Muller, R., & Rangelov, T. (2014b). *Dynamic Fracture of Piezoelectric Materials. Solutions of Time-harmonic problems via BIEM*. Solid Mechanics and its Applications, Vol. 212. Switzerland: Springer.
- Dineva, P., Rangelov, T., & Gross, D. (2005). BIEM for 2D steady-state problems in cracked anisotropic materials. *Engineering Analysis with Boundary Elements*, 29, 689–698.
- Dineva, P., Rangelov, T., Manolis, G., & Wuttke, F. (2014a). SH-wave scattering in the orthotropic half-plane weakened by cavities using BIEM. *Acta Acustica united with Acustica*, 100, 266–276.
- Dominguez, J. (1993). *Boundary elements in dynamics*. Southampton: Computational Mechanics Publications.
- Dong, C. Y. (2012). An integral equation formulation of two- and three- dimensional nanoscale inhomogeneities. *Computational Mechanics*, 49, 309–318.
- Dong, C. Y., & Pan, E. (2011). Boundary element analysis of nanoinhomogeneities of arbitrary shapes with surface and interface effects. *Engineering Analysis with Boundary Elements*, 35, 996–1002.

- Eshelby, J. D., Read, W. T., & Shockley, W. (1953). Anisotropic elasticity with applications to dislocation theory. *Acta Metallurgica*, 1, 251–259.
- Fang, X. Q., Liu, J. X., Yang, S. P., & Zhang, L. L. (2010). Effect of surface/interface on the dynamic stress of two interacting cylindrical nano-inhomogeneities under compressional waves. *Thin Solid Films*, 518, 6938–6944.
- Garcia-Sanchez, F. G. (2005). *Numerical study of fracture problems in elastic anisotropic and piezoelectric solids* (PhD thesis). University of Sevilla, Spain.
- Garcia-Sanchez, F., Saez, A., & Dominguez, J. (2006). Two-dimensional time-harmonic BEM for cracked anisotropic solids. *Engineering Analysis with Boundary Elements*, 30, 88–99.
- Grekov, M. A., & Morozov, N. (2012). Surface effects and problems of nanomechanics. *Journal of Ningbo University*, 25, 60–63.
- Gurtin, M. E., & Murdoch, A. I. (1975). A continuum theory of elastic material surfaces. *Archive for Rational Mechanics and Analysis*, 57, 291–323.
- Gurtin, M. E., & Murdoch, A. I. (1978). Surface stress in solids. *International Journal of Solids and Structures*, 14, 431–440.
- Gurtin, M. E., Weissmuller, J., & Larche, F. (1998). A general theory of curved deformable interfaces in solids at equilibrium. *Philosophical Magazine A*, 78, 1093–1109.
- Jammes, M., Mogilevskaya, S., & Crouch, S. (2009). Multiple circular nano-inhomogeneities and/or nano-pores in one of two joined isotropic half-planes. *Engineering Analysis with Boundary Elements*, 33, 233–248.
- Meguid, S. A., & Wang, X. D. (1995). The dynamic interaction of a crack with a circular cavity under anti-plane loading. *Journal of the Mechanics and Physics of Solids*, 43, 1857–1874.
- Mogilevskaya, S. G., Crouch, S. L., & Stolarski, H. K. (2008). Multiple interacting circular nano-inhomogeneities with surface/interface effects. *Journal of the Mechanics and Physics of Solids*, 56, 2298–2327.
- Ohyoshi, T. (1973). Effect of orthotropy on singular stresses for a finite crack. *Journal of Applied Mechanics*, 40, 491–497.
- Parvanova, S., Manolis, G., & Dineva, P. (2015). Wave scattering by nanoheterogeneities embedded in an elastic matrix via BEM. *Engineering Analysis with Boundary Elements*, 56, 57–69.
- Parvanova, S., Vasilev, G., Dineva, P., & Manolis, G. (2016). Dynamic analysis of nanoheterogeneities in a finite-sized solid by boundary and finite element methods. *International Journal of Solids and Structures*, 80, 1–18.
- Rizov, V. (2014). Fracture in foam core composite sandwich beams under mixed-mode I/II/III loading conditions. *Strength, Fracture and Complexity*, 8, 153–165.
- Rizov, V. (2015). Non-linear analysis of double cantilever beam. *Strength, Fracture and Complexity*, 9, 149–160.
- Ru, Y., Wang, G. F., & Wang, T. J. (2009). Diffraction of elastic waves and stress concentration near a cylindrical nano-inclusion incorporating surface effect. *Journal of Vibration and Acoustics*, 13, 061011-1–061011-7.
- Voigt, W. (1910). *Lehrbuch der Kristallphysik* [Textbook on crystal physics]. Leipzig: B. G. Teubner.
- Wang, G. F. (2009). Multiple diffraction of plane compressional waves by two circular cylindrical holes with surface effects. *Journal of Applied Physics*, 105, 013507-1–013507-6.
- Wang, C. Y., & Achenbach, J. D. (1994). Elastodynamic fundamental solutions for anisotropic solids. *Geophysical Journal International*, 118, 384–392.
- Wang, G. F., Wang, T. J., & Feng, X. Q. (2006). Surface effects on the diffraction of plane compressional waves by a nanosized circular hole. *Applied Physics Letters*, 89, 231923-1–231923-3.

Zhang, Q. F., Wang, G. F., & Schiavone, P. (2011). Diffraction of plane compressional waves by an array of nanosized cylindrical holes. *Journal of Applied Mechanics*, 78, 021003-1–021003-5.

## Appendix A. Time-Harmonic Fundamental Solution for 2D Anisotropic Domain

The frequency-dependent fundamental solution  $U_{ij}^*(\mathbf{x}, \boldsymbol{\xi}, \omega)$  for infinite domain of general anisotropy satisfies the following partial differential equations:

$$\begin{aligned} c_{11}U_{1i,11}^* + c_{66}U_{1i,22}^* + 2c_{16}U_{1i,12}^* + c_{16}U_{2i,11}^* + c_{26}U_{2i,22}^* + \\ + (c_{12} + c_{66})U_{2i,12}^* + \rho\omega^2U_{1i}^* = -\delta(\mathbf{x} - \boldsymbol{\xi})\delta_{1i} \\ c_{16}U_{1i,11}^* + c_{26}U_{1i,22}^* + (c_{12} + c_{66})U_{1i,21}^* + c_{66}U_{2i,11}^* + \\ + c_{22}U_{2i,22}^* + 2c_{26}U_{2i,12}^* + \rho\omega^2U_{2i}^* = -\delta(\mathbf{x} - \boldsymbol{\xi})\delta_{2i} \end{aligned} \quad (A1)$$

This fundamental solution is derived analytically in Wang and Achenbach (1994) by applying the Radon transform and its mathematical form is given below:

$$U_{ij}^*(\mathbf{x}, \boldsymbol{\xi}, \omega) = \frac{1}{4\pi^2} \int_{|\mathbf{m}|=1} \begin{pmatrix} g_1^1 & g_2^1 \\ g_1^2 & g_2^2 \end{pmatrix} \begin{pmatrix} g_1^1 \tilde{u}_1 & g_1^2 \tilde{u}_1 \\ g_2^1 \tilde{u}_2 & g_2^2 \tilde{u}_2 \end{pmatrix} \Big|_{s=|\langle \mathbf{x} - \boldsymbol{\xi}, \mathbf{m} \rangle|} \mathbf{d}\mathbf{m} \quad (A2)$$

Where:  $s = |\chi|$ ;  $\chi = \langle \mathbf{x} - \boldsymbol{\xi}, \mathbf{m} \rangle$ ;  $\langle \dots, \dots \rangle$  means scalar product,  $\tilde{u}_j(s, \mathbf{m})$  is presented by (A3):

$$\tilde{u}_j(s, \mathbf{m}) = \frac{1}{2a_j} \left\{ i\pi e^{ik_j s} - 2 \left[ ci(k_j s) \cos(k_j s) + si(k_j s) \sin(k_j s) \right] \right\} \quad (A3)$$

Where:  $\mathbf{m} = (m_1, m_2) = (\cos\varphi, \sin\varphi)$  is a unit vector describing the position along the unit circle,  $\varphi$  is the polar angle,  $a_j$  and  $g_i^j$ ,  $i, j = 1, 2$  are the eigenvalues and eigenvectors of the Christoffel matrix defined as

$$\mathbf{C}(\mathbf{m}) = \begin{bmatrix} c_{11}m_1^2 + c_{66}m_2^2 + 2c_{16}m_1m_2 & c_{16}m_1^2 + c_{26}m_2^2 + (c_{12} + c_{66})m_1m_2 \\ c_{16}m_1^2 + c_{26}m_2^2 + (c_{12} + c_{66})m_1m_2 & c_{66}m_1^2 + c_{22}m_2^2 + 2c_{26}m_1m_2 \end{bmatrix} \quad (A4)$$

i.e.  $a_j$  and  $g_i^j$  are solutions of the homogeneous system of Equations (A5):

$$[\mathbf{C} - a_j \mathbf{I}] \mathbf{g}_j = \mathbf{0} \quad (A5)$$

Here  $\mathbf{I}$  is the identity matrix and  $a_j(\mathbf{m}) = \rho(C_j(\mathbf{m}))^2$ ,  $C_j(\mathbf{m})$  are the phase velocities and the wave numbers are  $k_j(\mathbf{m}) = \omega/C_j(\mathbf{m})$ . Also we note that  $ci(s) = -\int_s^\infty \frac{\cos y}{y} dy$  and  $si(s) = -\int_s^\infty \frac{\sin y}{y} dy$  are the cosine and sine integrals.

The logarithmic singularity of the function  $\tilde{u}_j(s, \mathbf{m})$  is removed by means of the addition and subtraction of the term  $\ln(s)/a_j$ . In such a way, both displacement FS ( $U_{ij}^*(\mathbf{x}, \boldsymbol{\xi}, \omega)$ ) and its corresponding traction FS ( $T_{ij}^*(\mathbf{x}, \boldsymbol{\xi}, \omega)$ ) are decomposed into regular and singular parts (Wang & Achenbach, 1994; Garcia-Sanchez, 2005; Garcia-Sanchez et al., 2006). The later parts do not depend on frequency and correspond to the elastostatic FS whose explicit form for the anisotropic solid was obtained by Eshelby, Read, and Shockley (1953). The singular part of the displacement FS,  $U_{ij}^*(\mathbf{x}, \boldsymbol{\xi}, \omega)$ , and elastostatic FS are only different by a constant terms given in Denda, Wang, and Yong (2003). Detailed description of this decomposition could be found in Garcia-Sanchez (2005). When the static FS are calculated over an element containing the collocation point the displacement-based kernels exhibit a weak singularity of  $O(\ln r)$ , while the traction-based kernels exhibit a strong singularity of  $O(1/r)$ . The

integrals with weak singularity are computed using appropriate quadrature rules, while the strongly singular ones are evaluated by the rigid body motion concept. All regular parts of the integrals are calculated using numerical integration and standard Gaussian quadratures. The order of integration is first along the unit circumference by using 64 integration points followed by integration over the boundary element by using 10 integration points which is accurately enough for dimensionless frequency up to  $\Omega = \omega d \sqrt{\rho/c_{66}} = 1$ .

The authors BIEM numerical scheme uses the described above fundamental solution, but with the following expression for the function  $\tilde{u}_j(s, \mathbf{m})$ , given in (A6), because only in this form the fundamental solution for isotropic case is fully recovered.

$$\tilde{u}_j(s, \mathbf{m}) = \frac{1}{2a_j} \left\{ i\pi e^{ik_j s} + \pi \sin(k_j s) - 2 \left[ ci(k_j s) \cos(k_j s) + si(k_j s) \sin(k_j s) \right] \right\} \quad (\text{A6})$$

It could be verified that the above expression with the additional term  $+\pi \sin(k_j s)/(2a_j)$  (in comparison with Equation (A3)) satisfies the governing partial differential Equation (A1) which means that it is its fundamental solution.